Available online at www.sciencedirect.com
ScienceDirect
Trans. Nonferrous Met. Soc. China 34(2024) 2108−2119
Transactions of Nonferrous Metals Society of China
www.tnmsc.cn

Microstructure and mechanical properties of 7075 aluminum alloy prepared by metal fused deposition modeling

Yi SUN, Zhong-huai YI, Ting SHEN, Hui-wen XIONG, Xiao KANG, Lei ZHANG, Ke-chao ZHOU

State Key Laboratory of Powder Metallurgy, Central South University, Changsha 410083, China

Received 16 February 2023; accepted 21 September 2023

Abstract: An optimized microcrystalline wax-based feedstock was used to fabricate 3D 7075 Al alloy through metal fused deposition modeling (Metal-FDM). The affinity between the wax-based binders and powders was evaluated by a hot-press experiment. The phases, morphology evolution, tensile strength and friction performance of the sintered Al alloy were studied. The feedstock displayed shear-thinning behavior for a smooth extrusion process, resulting in a satisfactory surface quality and minimal stacking pores in the 3D structure. The morphology evolution of Al alloy sintered in nitrogen could be divided into four stages, including the precipitation of fine Mg_2Si and Si at 500 °C, appearance of Mg_2Si phase over 560 °C, nitridation of the oxide layers on alloy powders and enhanced grain growth via the diffusion process over 620 °C. The 3D 7075 Al alloys achieved a high relative density of 95%, exhibiting a tensile strength ranging from 120 to 141 MPa and a tensile strain of 1.0%−2.5%.

Key words: 7075 aluminum alloy; metal fused deposition modeling; metal injection molding; microstructure evolution; mechanical property

1 Introduction

Aluminum (Al) alloy is a non-ferrous metal that is widely used in the aerospace industry due to its high specific strength and good corrosion resistance [1]. The 7 series of Al alloys, particularly the 7075 Al alloy, exhibit higher specific strength and are important structural materials used in various industries [1]. In contrast, the powder metallurgy (PM) structural parts used in the automobiles are mainly focused on sintered iron-based parts [2]. Compared to iron-based alloys, Al alloys have only about a third of their density, higher specific strength, better corrosion resistance, and no magnetism.

Due to the increased demand for light weight and structural complexity, high-performance aluminum alloys are currently being developed [3]. Although the consumption of Al alloy parts by PM continues to grow, the PM route can only produce relatively simple parts with limited structure [4]. Metal 3D printing technology has emerged as an important and suitable method for producing complex parts [3,5]. Many additive manufacturing (AM) methods on 3D Al alloys have been reported, which were mainly focused on laser powder bed fusion (LPBF) process [6−8], wire arc additive manufacturing (WAAM) [9,10], and additive friction stir deposition process [11]. Due to the presence of hot cracks in the aluminum alloy prepared by LPBF during the construction process, only several Al alloys designed via eutectic solidification strategy were gradually developed, like Al−Si [12], Al−Fe [7] and Al−Ce [13] alloys. Although 3D Al alloys with enhanced strength and

Corresponding author: Hui-wen XIONG, Tel: +86-15387311652, E-mail: huiwenxiong@csu.edu.cn;
Xiao KANG, Tel: +86-15116260330, E-mail: kangxiao0601@csu.edu.cn
DOI: 10.1016/S1003-6326(24)66528-3

decreased hot cracks could be achieved via adding Sc and Zr elements, the intermetallic phases and precipitations were complicated, and heterogeneous microstructure was hard to control [14,15]. Compared to LPBF, WAAM [9] and additive friction stir deposition process [11] were more suitable for fabricating large-scale parts with lower residue stress and a higher deposition rate. Moreover, Al alloys including 2xxx Al−Cu [16], 4xxx Al−Si [17], 5xxx Al−Mg [17] and 7xxx Al−Zn [18] alloys have been successfully fabricated. However, the surface quality was poor due to the thick deposited layers.

Recently, metal fused deposition molding (Metal-FDM) using highly filled polymers as the feedstock has shown great potential to fabricate 3D metals [19]. The process involves printing a 3D green body via extrusion of the melted feedstock, layer by layer, on a heated platform. A dense structure is then achieved through subsequent debinding and sintering processes. Many types of 3D metals, such as steel [20], copper [21], titanium [22], nickel [23], tungsten-based alloys [24], ceramics of alumina [25], zirconia [26], and even composites like cemented carbides [27] have been successfully prepared, exhibiting acceptable properties. Overall, compared to other AM methods, Metal-FDM has several main advantages [19]: (1) small residual stress during printing; (2) uniform microstructure achieved through the debinding and sintering process; (3) low cost of the printing equipment and materials; (4) a wider range of printing materials that can be fabricated via the PM route; (5) mature technology support from powder metallurgy and metal injection molding. To date, less literature concerning Metal-FDM of Al alloy is available, likely due to the difficulty of the sintering process caused by the oxide layer on the surface of Al particles. QIU et al [28] studied the sintering densification process of Al−Mg alloy in flowing nitrogen. The sintering densification process could be divided into three stages, which included the breaking of oxide film via the diffusion of Mg at 460 °C, the formation of intermetallic compounds like Al_2Cu from 460 to 560 °C and the rapid densification process with grain growth from 560 to 600 °C, respectively. DU et al [29] prepared the 2 series Al alloy via MIM, with a high relative density over 98% and high tensile strength around 350 MPa after solution via adding the sintering aid of 0.5 wt.% Sn.

Based on this, 3D 7075 Al alloys were fabricated by Metal-FDM using an optimized wax-based feedstock. The rheological properties of the feedstock, phases and morphology evolution during sintering were characterized in detail.

2 Experimental

The Al−Zn−Mg−Cu alloy powders used in this study were purchased from Shanghai Xiangtian Nanomaterials Co. Ltd. (China). The composition of these powders included 5.5 wt.% Zn, 2.4 wt.% Mg, 1.5 wt.% Cu, 0.5 wt.% Fe, and 0.4 wt.% Si, with a diameter of approximately 10 μm. The microcrystalline wax (MW, CAS: 8001-75-0, Macklin, Shanghai, China) was used as the filler of the binder system. In order to optimize the binder component, backbone binders such as polypropylene (PP, CAS: 9003-07-0, Macklin, Shanghai, China), high-density polyethylene (HDPE, CAS: 9002-88-4, Macklin, Shanghai, China) and ethylene-vinyl acetate copolymer (EVA, CAS: 24937-78-8, Merck, Germany) were selected. A small amount of surfactant was adopted to enhance the bonding strength between the powders and polymers, which included stearic acid (SA, CAS: 57-11-4, Sinopharm, Shanghai, China) and zinc stearate (Znst, CAS: 557-05-1, Sinopharm, Shanghai, China).

The hot-pressing experiment was designed to evaluate the affinity between the binder and 7075 Al alloy powders. An increased affinity would result in denser samples after cooling. In order to optimize the binder system for smooth printing, three types of powder−polymer mixtures with different backbone binders were utilized in the hot-pressing process. These mixtures were prepared by ball milling Al powders and crushed binders for 2 h, maintaining a consistent solid loading of 68 vol.%. The binder system typically consisted of 60 wt.% MW, 35 wt.% backbone binders, 3 wt.% SA, and 2 wt.% Znst. For comparison, the backbone binders were selected as 35 wt.% PP, 35 wt.% HDPE, and 30wt.%HDPE-5wt.%EVA, respectively. The hot-pressing experiment followed the following steps: Firstly, the powder−polymer mixture was poured into the mold and subjected to a pressing pressure of 50 MPa. Secondly, the mold was heated to a certain temperature (190 °C for PP and 160 °C for

HDPE and HDPE−EVA) and held for 15 min. Then, the mold was cooled to room temperature. The resulting pressed cylinders were used to optimize the binder system.

The Metal-FDM process flow chart for Al alloys using MIM feedstocks consisted of five steps, as shown in Fig. 1, including kneading of the powder and polymer mixture, granulating the composite dough into pellets, Metal-FDM of 3D green parts, solvent debinding, thermal debinding and sintering. The binders were composed of 60 wt.% MW, 30 wt.% HDPE, 5 wt.% EVA, 3 wt.% SA and 2 wt.% Znst. Prior to kneading, the 7075 Al alloy powders were subjected to vacuum drying at 80 °C for 12 h. The kneading process took place in a kneader (CF-3LKH, Cfine, Dongguan, Guangdong Province, China), with a mixing temperature and time of 160 °C and 60 min, respectively, and a rotation speed of 40 r/min. The resulting hot composite dough was then granulated using a granulator (CF-45, Cfine, Dongguan, Guangdong Province, China) at 110 °C. This granulation process produced feedstocks in the form of small cylinders with a diameter of 3 mm. Finally, 3D green Al samples were prepared using a Metal-FDM machine (UPS-556, Uprise 3D, Shenzhen, Guangdong Province, China).

The printing process began with the creation of 3D models by UG, which were then imported into the UPRISE3D (v2.5.17) software produced by Uprise 3D in the form of files. To ensure successful printing, the printing temperature was set at 150 °C with a hot bed temperature of 100 °C. Using a nozzle diameter of 0.6 mm and a layer height of 0.2 mm, the hot wind was utilized during printing to maintain a stable temperature within the working cavity and prevent sample warping. The deposition temperature was carefully controlled at 140−155 °C using a stainless steel nozzle with a diameter of 0.6 mm. The hot bed was kept at 100 °C, and the layer height and printing speed were 0.2 mm and 40 mm/s, respectively. The green body was debinded in n-heptane solution at 50 °C constantly for 24 h. After the debinding process, the green body was thoroughly dried before being placed in a tube furnace for thermal debinding and sintering. The specific process was as follows: (1) heating from room temperature to 450 °C at 2 °C/min and holding for 2 h; (2) gradually raising temperature up to 500 °C at 2 °C/min and holding for 2 h; (3) finally firing to the target temperature in the range of 560−630 °C and holding for 1 h before furnace cooling. Throughout the sintering process, high-purity nitrogen was used as a protective atmosphere, with a consistent gas flow rate of 200 mL/min.

The rheological properties of the MW-based feedstocks were measured using a rotational rheometer (Haake Mars 60, Thermo Electron, Germany). The complex viscosity and modulus of the feedstock under shear stress from 10 to 1000 Pa were measured at 145, 150 and 155 °C, respectively. To gain a deeper understanding of the phase evolution of 7075 Al powders and the pyrolysis of the feedstock, the thermal properties of 7075 Al alloy powders and the prepared MW-based feedstock were characterized using a TG−DSC (NETZSCH STA 2500, NETZSCH, Germany). The

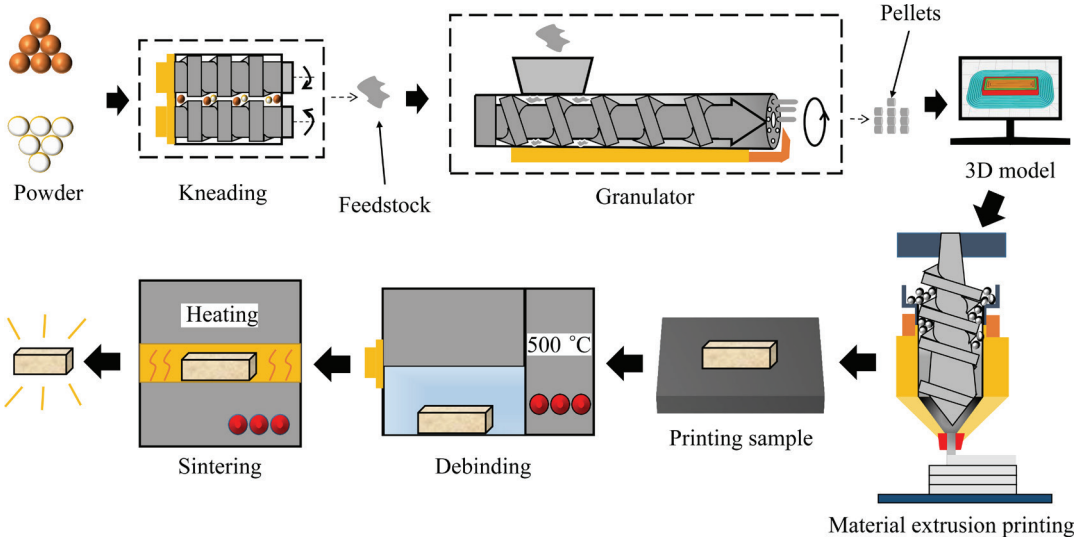

Fig. 1 Process flow chart of Metal-FDM of 7075 Al alloys

microstructure of powders, hot-pressed samples, extruded filaments, 3D structure and sintered alloys were observed by SEM (Mira3, Tescan, Czech). The sintering density of the alloy was measured by Archimedes principle, and the tensile properties were measured by universal strength testing machine (Instron3369, USA). Furthermore, an analysis of the phases after sintering was conducted using XRD (X'Pert Pro MPD, Nalytical, Finland).

3 Results and discussion

3.1 Characterization of 7075 Al alloy powders

The morphology and size of the raw powders are crucial in determining the viscosity of the feedstock and the sintering behavior of the printing samples [19,24]. Figure 2(a) demonstrates the spherical morphology of atomized 7075 Al alloy powders, with a grain size of approximately 10 μm. An advantage of these powders is the presence of partial irregular grains and fine grains, which contribute to an increase in packing density and strength of the green bodies. Figure 2(b) shows the TG−DSC curves of 7075 Al alloy powders fired in nitrogen environment. The DSC curve exhibits two endothermic peaks at 541.63 and 611.27 °C, which are attributed to the formation of intermetallic compounds of Al−Cu and Al−Si, respectively [28].

The affinity between the binders and 7075 Al alloy powders was assessed using the hot press technique. Hot-pressed samples in Figs. 3(c, f)

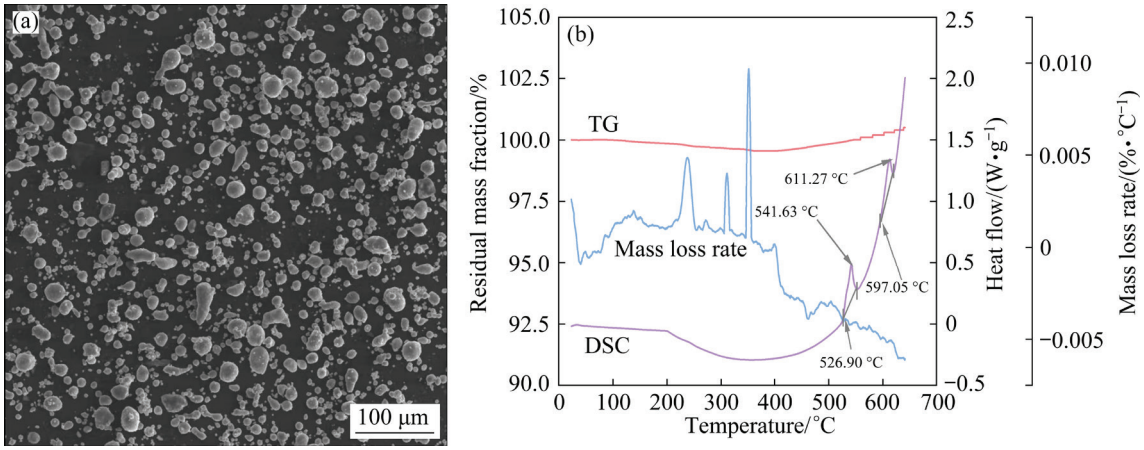

Fig. 2 SEM image (a) and TG−DSC curves (b) of atomized 7075 Al alloy powders

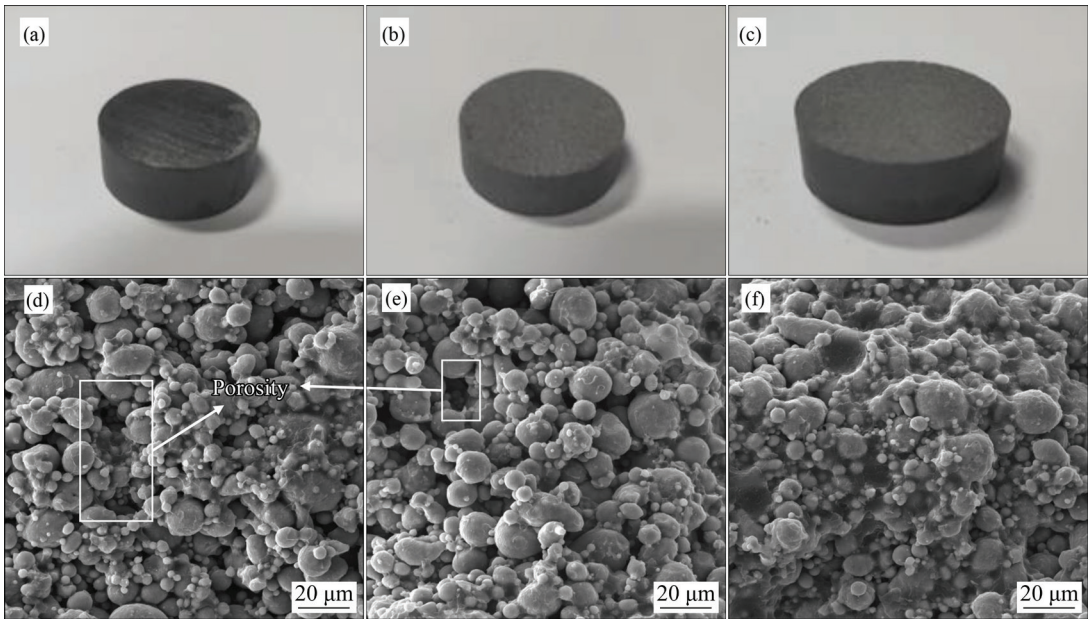

Fig. 3 Photos of hot-pressed green body (a−c) and SEM images of related fracture surface (d−f) with HDPE (a, d), PP (b, e) and HDPE−EVA (c, f) as backbone binders

exhibit the highest density, with no visible pores on the fracture surface. Meanwhile, Figs. 3(a, d) and 3(b, e) illustrate particles that have become detached from the binder skeleton, indicating unsatisfactory powder−binder affinity which affects the properties of the green body adversely. Therefore, MW-based binders, including HDPE−EVA, are found to effectively encapsulate the powders due to their excellent wettability with the polymers. The HDPE−EVA system was selected as the backbone binders for subsequent experiments, given that EVA can lubricate HDPE to encapsulate powders more effectively [30].

3.2 Morphology, thermal and rheological properties of feedstock

The as-prepared feedstock after kneading and granulating is shown in Fig. 4(a). The pellets had an irregular shape with a size around 3−5 mm and a smooth surface. The color of the feedstock was similar to that of 7075 Al alloy powder. Figure 4(b) displays the TG−DSC curves, which confirmed three endothermic peaks on the DSC curve. These peaks corresponded to the melting of MW at 80 °C, pyrolysis of MW at 332 °C, and HDPE−EVA at 454 °C. It is indicated that the mass loss of the feedstock began at 200 °C and was completed at 500 °C. At 500 °C, the binders were completely removed, resulting in a mass loss of 14%.

The rheology of the feedstock plays an important role in evaluating its viscoelastic properties and ensuring a smooth printing process. Temperature, being a key factor in printing, influences the complex modulus and viscosity of the microwave-based feedstock under varying shear stress conditions at 145, 150, and 155 °C. Figure 5 illustrates the relationship between complex viscosity (η) and shear stress (τ). It can be observed that the complex viscosity decreased with an increase in shear stress, indicating shear thinning behavior. Based on the value of τ, the rheological property can be divided into three stages. In the preliminary stage, at low τ, the storage modulus (G') was higher than the loss modulus (G''), suggesting that the feedstock exhibited the characteristics of an elastic solid with a viscosity higher than 10^5 Pa. As the τ increased towards the gel point, G' equaled G'', indicating a semisolid state. Higher temperatures caused the gel point to occur at lower τ values and slightly decreased the complex viscosity of the feedstock. When the shear stress was further increased, the rate of descent of G' became faster than the rate of descent of G'', indicating that the feedstock transformed into a viscoelastic liquid. During this stage, the viscosity decreased rapidly, ensuring smooth extrusion of the flowing feedstock through a small nozzle.

The phase structure of the elastic solid was disrupted with the increase in shear stress, leading to a transformation into a viscoelastic liquid. During the period of $G' > G''$, the descent rate of the composite viscosity is slower than the storage modulus and loss modulus. Nevertheless, during the period of $G' < G''$, the descent rate of the composite viscosity is clearly faster than that of the storage modulus and loss modulus. With the increasing of shear stress, the transformation of the feedstock from elastic solid to viscoelastic liquid and the decline in composite viscosity confirmed the shear-thinning characteristic of the feedstock. Herein, the values of shear stress at the gel point aid in evaluating the suitable temperature for stable printing. When $G'=G''$, the abscissa value of shear stress at 150 and 155 °C is smaller than that at 145 °C.

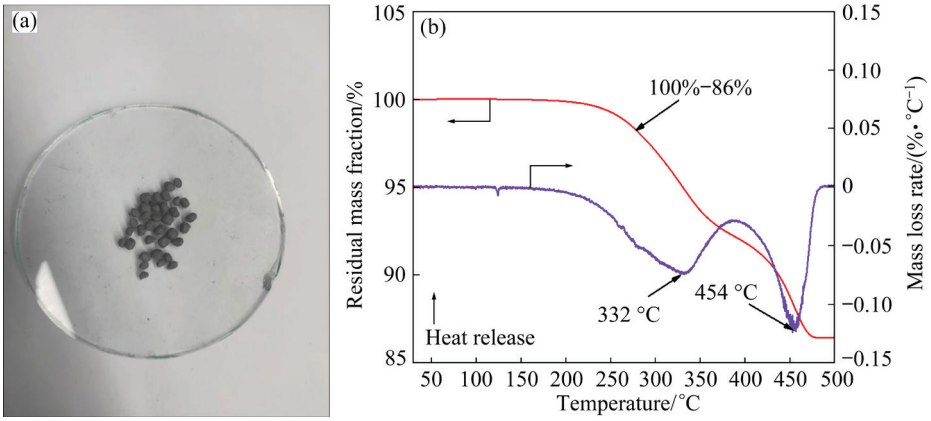

Fig. 4 Photos of MW-based feedstock (a) and related TG−DSC curves fired in nitrogen (b)

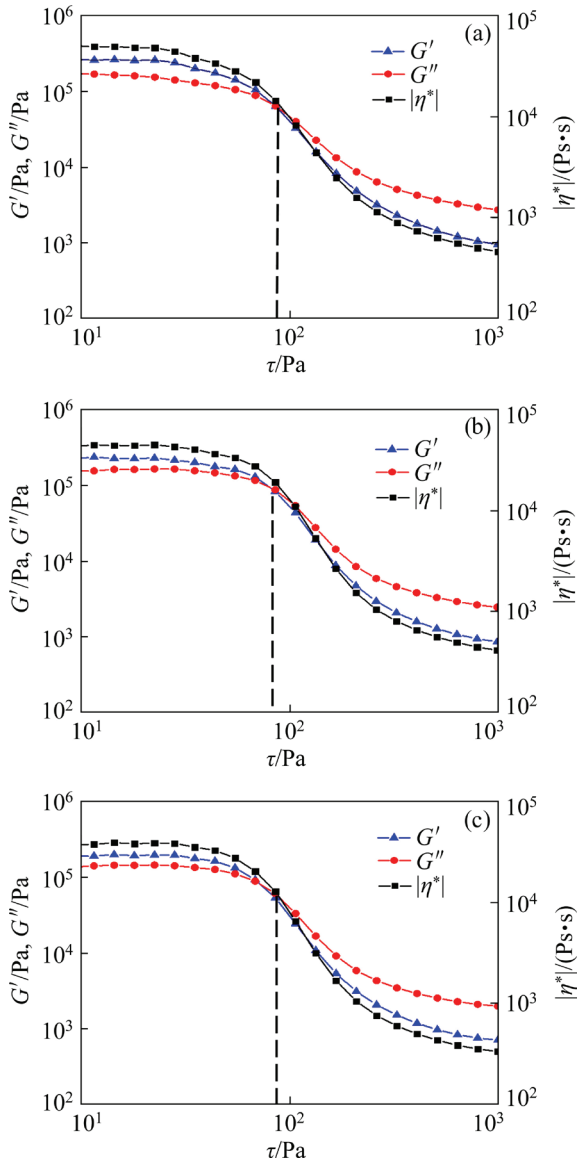

Fig. 5 Storage modulus (G'), loss modulus (G'') and complex viscosity (η*) of feedstock within shear stress (τ) from 10 to 1000 Pa at different temperatures (The binder system of feedstock was composed of 60 wt.% MW, 30 wt.% HDPE, 5 wt.% EVA, 3 wt.% SA, and 2 wt.% Znst): (a) 145 °C; (b) 150 °C; (c) 155 °C

Given that the microwave binder chosen for this experiment tended to stick to the nozzle above 150 °C, 150 °C was selected as the optimized printing temperature for this experiment.

3.3 Characterization of extruded filaments at different extrusion temperatures

The microstructure of the surface and fracture of the extruded filaments were investigated, as shown in Fig. 6. The SEM images in Figs. 6(a−d) revealed that the surface of the extruded filaments varied at different temperatures. At a high printing temperature, extruded filament exhibited a very smooth surface due to the low viscosity at the wall of nozzle. However, at lower temperatures, a rough surface with partially unwrapped Al powders was observed, suggesting an increase in viscosity and friction during the extrusion process. In terms of surface quality, the morphology of the filaments extruded at 140 and 145 °C was found to be inferior compared to that extruded at 150 and 155 °C. Furthermore, as shown in the insets of Figs. 6(c, d), the 7075 Al alloy powders were evenly dispersed within the polymers. Figures 6(e−l) display the fracture of extruded lines at different temperatures. Several defects could be found in Figs. 6(e, f), and the packaging of spherical powders in Figs. 6(i, j) was worse than that in Figs. 6(k, l). With taking the surface and fracture of the extruded lines into consideration, a printing temperature of 150 °C was deemed suitable, as it aligned well with the rheological properties of the feedstock.

3.4 Microstructure of as-printed 3D 7075 Al samples

Figures 7(a, b) show photos of the printed tensile samples and rotating nut. The stable printability of the MW-based feedstock was demonstrated by the production of solid green samples with excellent surface quality. The printing steps could be observed along the Z-axis direction due to the layer-by-layer deposition [31]. The surface, side, and fracture views of the as-printed tensile samples are presented in Fig. 7. Figures 7(c, d) confirmed the fine combination and connectivity between deposited layers, with the measured width and thickness of the layers being 600 and 200 μm, respectively. The connectivity between layers on the side explains that the filaments were extruded smoothly and steadily. In addition, Figs. 7(e, f) show a dense fracture surface with no stacking pores formed between layers, indicating satisfactory bonding between the polymers. The uniform dispersion of the 7075 Al alloy powders in the MW-based binder resulted in a pull-out of the spherical particles after fracture, leaving spherical pores in the composites. Overall, the green bodies of 7075 Al alloys exhibited high quality, including good surface accuracy, few stacking pores and a uniform microstructure.

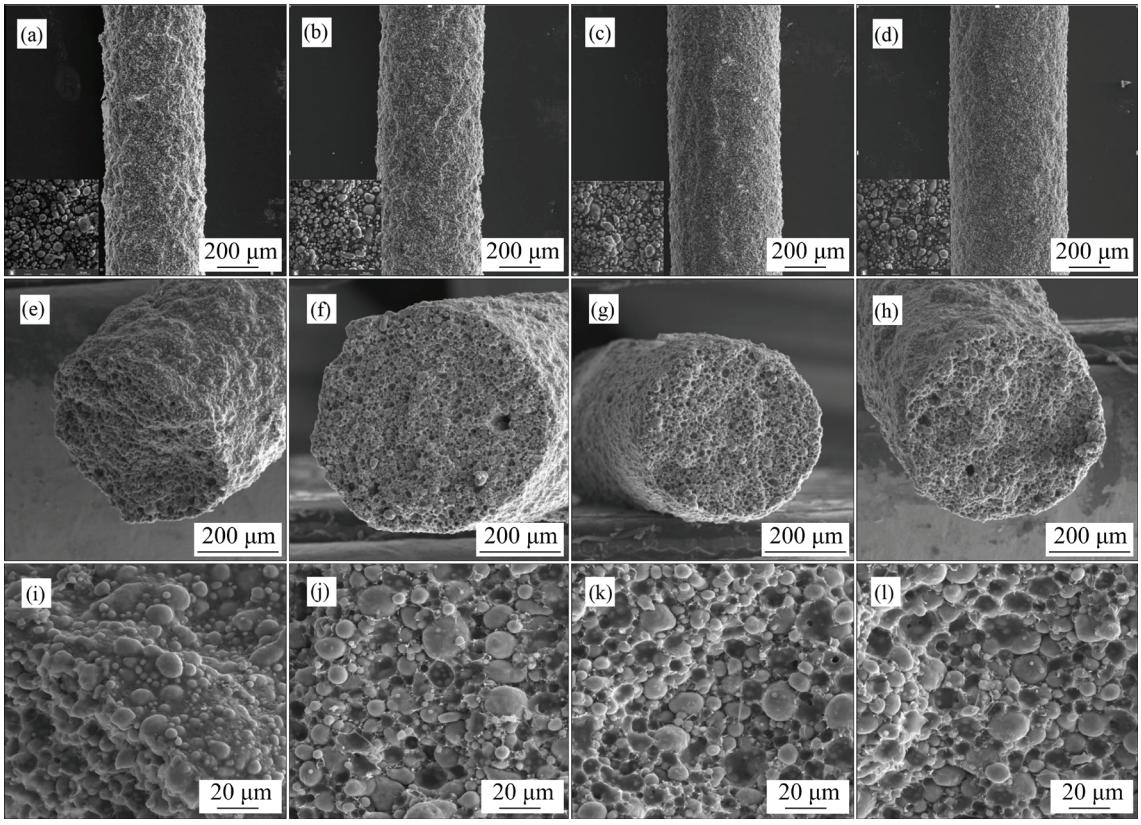

Fig. 6 Surface (a−d) and fracture (e−l) morphologies of extruded filaments at different extrusion temperature: (a, e, i) 140 °C; (b, f, j) 145 °C; (c, g, k) 150 °C; (d, h, l) 155 °C

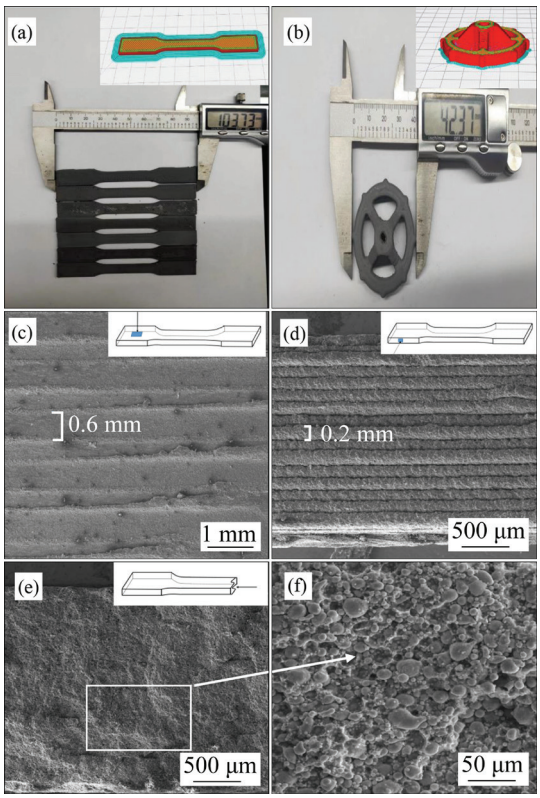

Fig. 7 Photos of CAD modes and as-printed tensile sample (a) and rotating nut (b); surface (c), side (d) and fracture (e, f) images of printing tensile samples

3.5 Debinding and sintering

MW, as the main binder, was firstly removed via solvent debinding. The process of solvent debinding was carried out in n-heptane solution at 50 °C. The wax was rapidly removed within the first 5 h, resulting in a mass loss of approximately 6.5%. After 24 h, the mass loss reached around 8%, as shown in Fig. S1(a) in Supporting Materials (SM). Figure 8 shows the SEM images and EDS mapping of the 3D Al alloys sintered at different temperatures ranging from 500 to 630 °C. As the sintering temperature increased, the density of the material first increased and then decreased. The relative density of the material reached its peak of 95% when the temperature reached 620 °C, as shown in Fig. S1(b) in SM. When the thermal debinding was finished at 500 °C, the binders are totally removed, leaving in-situ holes in the body. At a sintered temperature of 560 °C, there was a linear shrinkage of approximately 9% and clear grain boundaries of the spherical powders were observed. Hence, the diffusion among Al alloy particles was limited due to the stable oxide on the surface. At this stage, the nitridation of Al_2O_3 layers

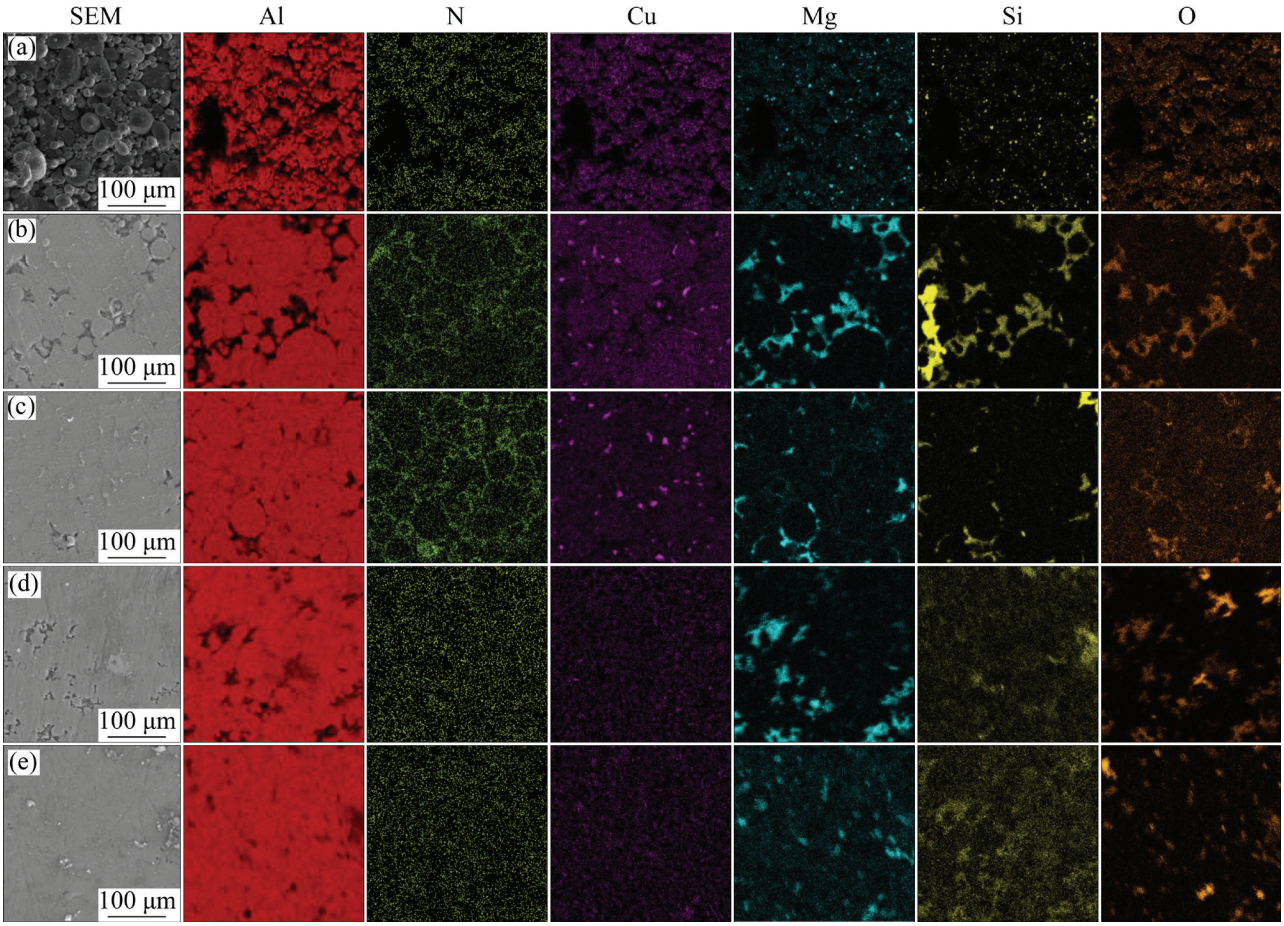

Fig. 8 SEM images, and element distributions of sintered 3D 7075 Al alloys at different temperatures: (a) 500 °C; (b) 560 °C; (c) 610 °C; (d) 620 °C; (e) 630 °C

was weak, and shrinkage primarily resulted from the formation of the Mg_2Si phase, leading to a decreased number of holes. Further increasing the sintering temperature to 610 °C, the number and size of holes were significantly reduced, and the linear shrinkage was increased to around 11%. A complete nitride was confirmed at this stage, along with the formation of sintering necks among Al particles. Moreover, liquid Al−Cu phase appeared, dispersing among Al alloy grains. Compared to the agglomerated Mg_2Si at 560 °C, the phases exhibited a tendency to disperse uniformly, possibly due to the enhanced wettability between the Al−Cu liquid and newly formed nitride layers. When the firing temperature was increased to 620 and 630 °C, samples with relative density over 95% were achieved, accompanied by a slight increase in grain size. Based on the EDS mapping results, three phases were confirmed, including the Al alloy matrix, Mg_2Si compound and precipitated Si. A certain amount of oxygen was bonded with Mg, which was probably introduced during the treatment.

By combining with the ESD mapping results in Fig. 8 and the XRD patterns in Fig. 9, the distribution of elements, phases and morphology evolution during the sintering process could be analyzed. Firstly, it could be analyzed that the dispersion of zinc and copper was relatively uniform, while the aggregation of magnesium, silicon and oxygen occurred. The phases produced during the sintering process were mainly Al, AlN, Si and Mg_2Si. It is worth noting that N occupied the lattice of Al to generate AlN, but no evidence of this was found in the XRD patterns due to the low crystallinity of the nano grains. Meanwhile, there are Al−Cu phases present, but their peaks were not clearly visible.

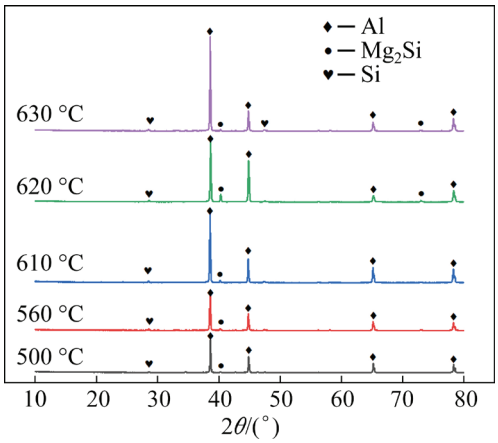

Fig. 9 XRD patterns of sintered 3D Al alloys at different temperatures

The process of microstructure evolution during sintering was divided into four stages. The first stage was the formation of Mg2Si and precipitation of Si, occurring over 500 °C. Secondly, complete nitrides were formed on the surface of Al alloy spherical grains, with the appearance of Al−Cu liquids. Then, the alloy grains started to be sintered together via diffusion process, resulting in the uniform dispersion of Cu and N. Finally, dense structure of 3D 7075 Al alloys was formed, with a few Mg_2Si and Si distributing among the Al alloy grains. Overall, AlN and Mg_2Si were formed at 500 °C, the Al−Cu phase was formed at 560 °C, and the change of phase was finished over 560 °C and remained unchanged. The specific reactions were expressed as follows [4,29]:

$$Al+N_2 \rightarrow AlN \quad (1)$$

$$Mg+Si \rightarrow Mg_2Si \ (500\ °C) \quad (2)$$

$$Al+Cu \rightarrow AlCu_3 \ (560\ °C) \quad (3)$$

During the sintering process, managing the oxygen content was of paramount importance. Excessive oxygen content could hinder the diffusion process within the Al-based matrix, leading to difficulties in shrinkage and poor performance. The fabrication of dense Al alloys relies on the disruption of the oxide layer on Al particles, which can be achieved through two routes during sintering. On the one hand, the oxide film is disrupted by bonding Mg atoms with the oxygen of the oxide. On the other hand, the nitridation process plays a crucial role in the destruction of the oxide film on the surface of Al. Hence, 3D 7075 Al alloys with dense structure and uniform morphology were obtained.

3.6 Mechanical and tribological properties

In this work, the solid-solution treatment was not considered. Instead, the main focus was on evaluating the basic morphology and tensile strength of the sintered 3D 7075 Al alloys. The tensile strength was in the range of 120−140 MPa, with a tensile strain from 1.0% to 2.5%, as shown in Fig. S2 in SM. Owing to a few residue pores, the strength was relatively lower than that of the deformed samples. Nevertheless, strengthening of the 3D Al alloys via gas-pressure sintering and subsequent heat treatment will be considered in future work. Figure 10 shows the SEM images of the fracture surface of tested tensile samples. The sintered samples had a grain size around 12 μm. Several dimples were confirmed, indicating a good toughening effect during the breaking. Meanwhile, a few pores could act as the source of fracture, leading to decreased strength.

The friction coefficient curves with different speeds are shown in Fig. 11(a). In the initial stage, the friction coefficient curves increased first and then decreased after reaching a peak. With an increase in the sliding distance, the friction coefficient curves kept constant. As the sliding speed increased, the wear rate of the material surface significantly increased. In comparison to lower sliding speeds, at a sliding speed of 0.8 m/s, there were fewer scratches present, but the width of these scratches was larger, as shown in Fig. S3 in SM. The average values of the friction coefficients and wear rates are presented in Fig. 11(b). The sliding speed had a slight effect on the average friction coefficient of the 7075 aluminium, and the average friction coefficients ranged from 0.52 to 0.64. With an increase in the sliding speed, the average friction coefficient increased first and then decreased. When the sliding speed reached 0.4 m/s, the maximum friction coefficient was 0.64. The sliding speed had a slight influence on the wear rates of the material. There was a slight increase in the wear rate from 0.1 to 0.2 m/s, reaching a maximum at a sliding speed of 0.2 m/s. With an increase in the sliding speed, the wear rate decreased and then stabilized. The lowest wear rate of the material was 4.5×10^{-7} mm/(N·m) in a high-purity nitrogen atmosphere.

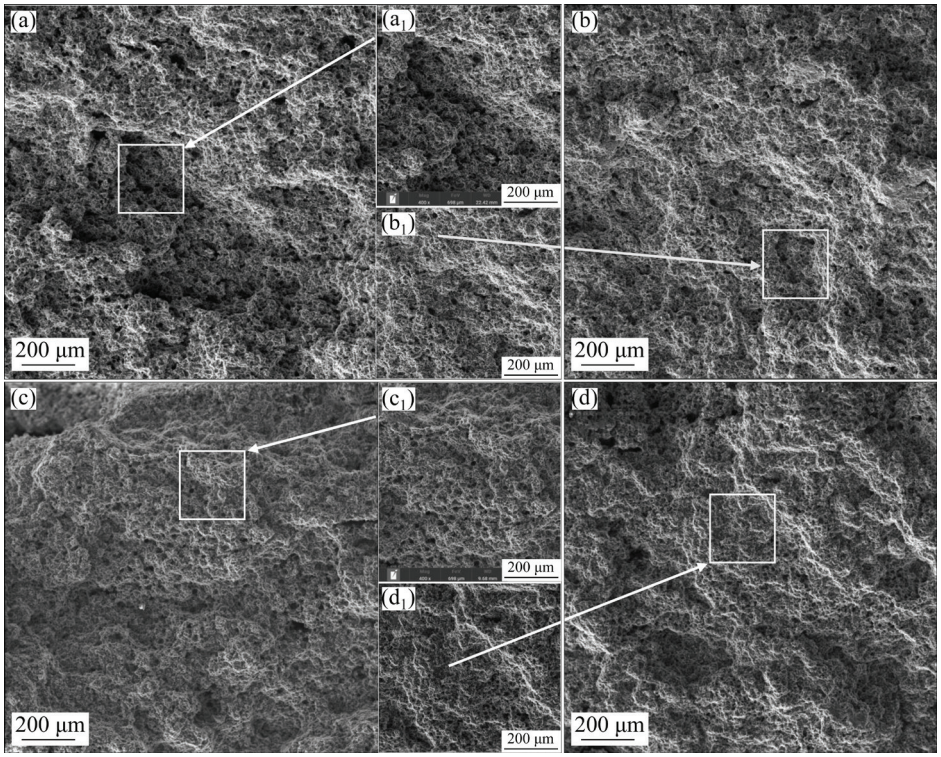

Fig. 10 SEM images of fracture surface of tensile samples after testing: (a) Sample 1; (b) Sample 2; (c) Sample 3; (d) Sample 4

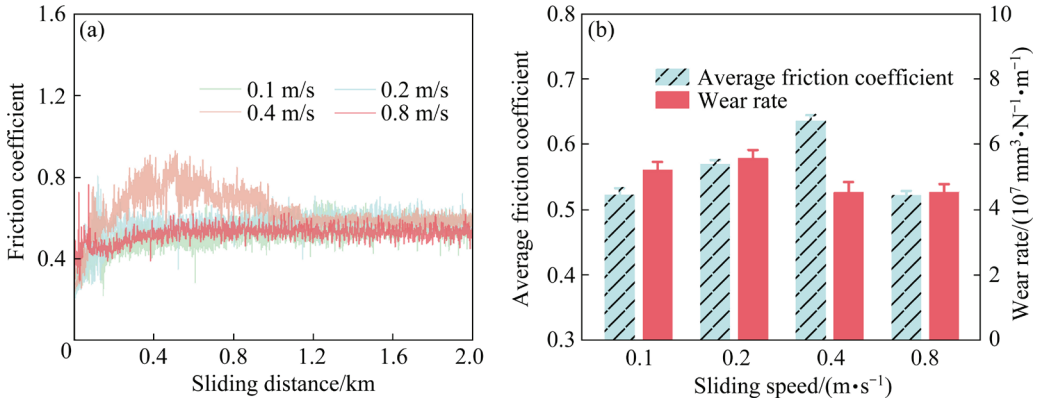

Fig. 11 Friction coefficient curves (a) and average friction coefficient and wear rates (b) of 7075 aluminium manufactured by FDM

4 Conclusions

(1) A hot-pressing experiment was designed to evaluate the affinity between CW-based binders and 7075 Al alloy powders. The optimized binder system exhibited shear thinning behavior and good wrapping property to the powders, which was composed of 60 wt.% MW, 30 wt.% HDPE, 5 wt.% EVA, 3 wt.% SA, and 2 wt.% Znst.

(2) Extruded filaments with smooth surface and dense structure were confirmed during printing at 150 °C, and 3D green samples with good surface quality and few stacking pores were achieved.

(3) Morphology evolution during sintering could be divided into four stages, including the precipitation of fine Mg_2Si and Si at 500 °C, the formation of liquid phase of Mg_2Si over 560 °C, nitridation of the oxide layers with the formation of $AlCu_3$ phase, and grain growth with improved density via the diffusion process at temperature over 620 °C. 3D 7075 Al alloys with a high relative density of 95% were fabricated after sintering, with a tensile strength of 141 MPa.

CRediT authorship contribution statement

Yi SUN: Conceptualization, Resources, Writing − Original draft; **Zhong-huai YI:** Validation, Methodology; **Ting SHEN:** Investigation, Formal analysis; **Hui-wen XIONG:** Funding acquisition, Writing − Reviewing & editing; **Xiao KANG:** Software, Data curation; **Lei ZHANG:** Project administration; **Ke-chao ZHOU:** Supervision.

Declaration of competing interest

The authors declare that they have no known competing financial interests or personal relationships that could have appeared to influence the work reported in this paper.

Acknowledgments

This research was supported by the National Key Research and Development Program of China (No. 2021YFB3701900).

Supporting Materials

Supporting Materials in this paper can be found at: http://tnmsc.csu.edu.cn/download/04-p2108-2023-0184-Supporting_materials.pdf.

References

[1] WEI Li-jun, HAN Bao-shuai, YE Fan, DITTA A, LI Long, XU Yan-jin, WU Su-jun. Influencing mechanisms of heat treatments on microstructure and comprehensive properties of Al−Zn−Mg−Cu alloy formed by spray forming [J]. Journal of Materials Research and Technology, 2020, 9(3): 6850−6858.

[2] KULKARNI H, DABHADE V V. Green machining of powder-metallurgy-steels (PMS): An overview [J]. Journal of Manufacturing Processes, 2019, 44: 1−18.

[3] ABOULKHAIR N T, SIMONELLI M, PARRY L, ASHCROFT L, TUCK C, HAGUE R. 3D printing of Aluminium alloys: Additive manufacturing of aluminium alloys using selective laser melting [J]. Progress in Materials Science, 2019, 106: 100578.

[4] WANG Tao, HUANG Yu-feng, YANG Lun, MA Yun-zhu, LIU Chao, WU Lei, YAN Huan-yuan, ZHAO Xin-yue, LIU Wen-sheng. Microstructure and mechanical properties of 7055 Al alloy prepared under different sintering conditions using powder by-products [J]. Materials Science and Engineering A, 2021, 805: 140562.

[5] BABU V V P, GB V K. A review on 3D printing process on metals and their surface roughness and dimensional accuracy [J]. Materials Today: Proceedings, 2022, 64: 523−530.

[6] MISHRA R S, THAPLIYAL S. Design approaches for printability-performance synergy in Al alloys for laser-powder bed additive manufacturing [J]. Materials & Design, 2021, 204: 109640.

[7] QI Xing, TAKATA N, SUZUKI A, KOBASHI M, KATO M. Controllable tensile performance of additively manufactured Al−Fe alloy [J]. Materials Science and Engineering A, 2022, 855: 143893.

[8] SCHLIEPHAKE D, LOPES C, EGGELER Y M, CHEN H, FREUDENBERGER J, BAYOUMY D, HUANG A J, KAUFFMANN A. Improved work hardening capability and ductility of an additively manufactured and deformed Al−Mn−Mg−Sc−Zr alloy [J]. Journal of Alloys and Compounds, 2022, 924: 166499.

[9] REN Xue-lei, JIANG Xiao-qing, YUAN Tao, ZHAO Xiao-hu, CHEN Shu-jun. Microstructure and properties research of Al−Zn−Mg−Cu alloy with high strength and high elongation fabricated by wire arc additive manufacturing [J]. Journal of Materials Processing Technology, 2022, 307: 117665.

[10] WANG Zu-heng, GAO Yi-feng, HUANG Jia-lin, WU Chuan-dong, WANG Gui-lan, LIU Jing. Precipitation phenomena and strengthening mechanism of Al−Cu alloys deposited by in-situ rolled wire-arc additive manufacturing [J]. Materials Science and Engineering A, 2022, 855: 143770.

[11] BECK S C, RUTHERFORD B A, AVERY D Z, PHILLIPS B J, RAO H, REKHA M Y, BREWER L N, ALLISON P G, JORDON J B. The effect of solutionizing and artificial aging on the microstructure and mechanical properties in solid-state additive manufacturing of precipitation hardened Al−Mg−Si alloy [J]. Materials Science and Engineering A, 2021, 819: 141351.

[12] CHEN Yang, ZHANG Jun-xi, GU Xin-hui, DAI Nian-wei, QIN Peng, ZHANG Lai-chang. Distinction of corrosion resistance of selective laser melted Al−12Si alloy on different planes [J]. Journal of Alloys and Compounds, 2018, 747: 648−658.

[13] ZHOU Le, HUYNH T, PARK S, HYER H, MEHTA A, SONG Shu-tao, BAI Yuan-li, MCWILLIAMS B, CHO K, SOHN Y. Laser powder bed fusion of Al−10wt.%Ce alloys: Microstructure and tensile property [J]. Journal of Materials Science, 2020, 55: 14611−14625.

[14] MARTIN J H, YAHATA B D, HUNDLEY J M, MAYER J A, SCHAEDLER T A, POLLOCK T M. 3D printing of high-strength aluminium alloys [J]. Nature, 2017, 549(7672): 365−369.

[15] THAPLIYAL S, KOMARASAMY M, SHUKLA S, ZHOU Le, HYER H, PARK S, SOHN Y, MISHRA R S. An integrated computational materials engineering-anchored closed-loop method for design of aluminum alloys for additive manufacturing [J]. Materialia, 2020, 9: 100574.

[16] WANG Zhen-nan, LIN Xin, WANG Li-ling, CAO Yang, ZHOU Ying-hui, HUANG Wei-dong. Microstructure evolution and mechanical properties of the wire+ arc additive manufacturing Al−Cu alloy [J]. Additive Manufacturing, 2021, 47: 102298.

[17] KÖHLER M, FIEBIG S, HENSEL J, DILGER K. Wire and arc additive manufacturing of aluminum components [J]. Metals, 2019, 9(5): 608.

[18] DONG Bo-lun, CAI Xiao-yu, LIN San-bao, LI Xiao-long, FAN Cheng-lei, YANG Chun-li, SUN Hao-ran. Wire arc additive manufacturing of Al−Zn−Mg−Cu alloy:

Microstructures and mechanical properties [J]. Additive Manufacturing, 2020, 36: 101447.
[19] GONZALEZ-GUTIERREZ J, CANO S, SCHUSCHNIGG S, KUKLA C, SAPKOTA J, HOLZER C. Additive manufacturing of metallic and ceramic components by the material extrusion of highly-filled polymers: A review and future perspectives [J]. Materials, 2018, 11(5): 840.
[20] THOMPSON Y, GONZALEZ-GUTIERREZ J, KUKLA C, FELFER P. Fused filament fabrication, debinding and sintering as a low cost additive manufacturing method of 316L stainless steel [J]. Additive Manufacturing, 2019, 30: 100861.
[21] SINGH G, MISSIAEN J M, BOUVARD D, CHAIX J M. Copper extrusion 3D printing using metal injection moulding feedstock: Analysis of process parameters for green density and surface roughness optimization [J]. Additive manufacturing, 2021, 38: 101778.
[22] SINGH P, BALLA V K, TOFANGCHI A, ATRE S V, KATE K H. Printability studies of Ti−6Al−4V by metal fused filament fabrication (MF3) [J]. International Journal of Refractory Metals and Hard Materials, 2020, 91: 105249.
[23] FILIP P, HAUSNEROVA B, HNATKOVA E. Continuous rheological description of highly filled polymer melts for material extrusion [J]. Applied Materials Today, 2020, 20: 100754.
[24] HU Zhang-ping, LIU Ye, QIAN Zhu, ZHAO Ya-nan, DONG Ji, YANG Zhen-wen, WANG Zu-min, MA Zong-qing. The preparation of high-performance 96W−2.7Ni−1.3Fe alloy parts by powder extrusion 3D printing [J]. Materials Science and Engineering A, 2021, 817: 141417.
[25] NÖTZEL D, HANEMANN T. New feedstock system for fused filament fabrication of sintered alumina parts [J]. Materials, 2020, 13(19): 4461.
[26] HE Qing-long, JIANG Jie, YANG Xian-feng, ZHANG Li, ZHOU Zhe, ZHONG Yuan, SHEN Zhi-jian. Additive manufacturing of dense zirconia ceramics by fused deposition modeling via screw extrusion [J]. Journal of the European Ceramic Society, 2021, 41(1): 1033−1040.
[27] DONG Ming-ye, ZHAO Yue, LI Quan, WANG Fu-de, WU Ai-ping. Effects of Cd addition in welding wires on microstructure and mechanical property of wire and arc additively manufactured Al−Cu alloy [J]. Transactions of Nonferrous Metals Society of China, 2022, 32(3): 750−764.
[28] QIU Ting-ting, WU Mao, DU Zhi-yuan, QU Xuan-hui. Sintering densification process of powder metallurgy aluminum alloy [J]. Chinese Journal of Engineering, 2018, 40(9): 1075−1082. (in Chinese)
[29] DU Zhi-yuan, WU Mao, QIU Ting-ting, QU Xuan-hui. Metal injection molding of Al−Cu−Mg−Si alloy [J]. The Chinese Journal of Nonferrous Metals, 2019, 29(11): 2471−2480. (in Chinese)
[30] OSMAN H, LIU Lin. Additive manufacturing of high-entropy alloy composites: A review [J]. Transactions of Nonferrous Metals Society of China, 2023, 33(1): 1−24.
[31] SHEN Ting, XIONG Hui-wen, LI Zhi-you, ZHANG Lei, ZHOU Ke-chao. Fused deposition fabrication of high-quality zirconia ceramics using granular feedstock [J]. Ceramics International, 2021, 47(24): 34352−34360.

金属熔融沉积成型制备 7075 铝合金的显微组织和力学性能

孙 亿，易中怀，沈 廷，熊慧文，康 潇，张 雷，周科朝

中南大学 粉末冶金国家重点实验室，长沙 410083

摘 要：以优化后的微晶蜡基喂料为原料，通过金属熔融沉积成型制备 3D 7075 Al 合金。通过热压实验评估蜡基黏合剂和粉末之间的亲和力，研究烧结铝合金的物相、形态演变、拉伸强度和摩擦性能。打印喂料表现出剪切变稀行为，可使熔融挤出过程变流畅，并获得较好表面质量且含少量层间堆积孔隙的 3D 坯件。在氮气中烧结铝合金的形态演变可分为 4 个阶段，包括 500 ℃下 Mg_2Si 和 Si 的沉淀，560 ℃以上 Mg_2Si 的出现，合金粉末上氧化物层的氮化，以及 620 ℃以上通过扩散过程增强的晶粒生长。3D 7075 Al 合金的相对密度达 95%，拉伸强度为 120~141 MPa，拉伸应变为 1.0%~2.5%。

关键词：7075 铝合金；金属熔融沉积成型；金属注射成型；显微组织演变；力学性能

(Edited by Bing YANG)